

Intergalactic filaments spin

Qianli Xia,^{1*} Mark C. Neyrinck,^{2*} Yan-Chuan Cai^{1*}, Miguel A. Aragón-Calvo³

¹Institute for Astronomy, University of Edinburgh

Royal Observatory, Blackford Hill, Edinburgh, UK

²Ikerbasque, the Basque Foundation for Science; University of the Basque Country, Bilbao;
Donostia International Physics Center

³Instituto de Astronomía, UNAM, Apdo. Postal 106, Ensenada 22800, B.C., México

*To whom correspondence should be addressed;

E-mail: qx211@roe.ac.uk; Mark.Neyrinck@gmail.com; cai@roe.ac.uk; maragon@astro.unam.mx

April 27, 2022

Matter in the Universe is distributed in a cosmic web, with a filament of matter typically connecting neighboring galaxy pairs, separated by tens of millions of light-years. Filaments are known to influence the spins of galaxies around them, but it remains unknown whether filaments themselves spin. Here, we measure the angular momentum around intergalactic filaments in a dark-matter cosmological simulation, finding that matter generally rotates substantially around them. Our results suggest that spin is a fundamental property of filaments, part of a full picture of structure formation. Filaments are likely to be the longest coherently rotating objects in the Universe. This finding helps to explain how galaxies spin in the cosmic web, and could provide a mechanism to generate intergalactic magnetic fields.

The cosmic web of bubble-like voids, separated by walls, filaments and haloes, describes the matter distribution of our Universe on scales much larger than galaxies. It is predicted by the standard model of cosmology (1, 2) and observed in galaxy surveys (3–5). Intergalactic filaments are the skeletons of the cosmic web, generally connecting pairs of neighboring galaxies separated by over 10^7 light years (6, 7). They feed matter into forming galaxies, and are known

to influence the spins of nearby galaxies (8–15). But is filament spin substantial, necessary for a complete picture of structure formation in our Universe?

Filamentary rotation has only been speculated about before. In Refs. (16, 17), the authors suggested that wall intersections provide a swirling, rotating environment, aligning the spins of small haloes with filaments, but did not demonstrate filament spins directly. In a toy ‘origami approximation,’ galaxies spin if and only if filaments attached to them spin (18); this unusually art-inspired analogy suggests that filaments spin. Also, haloes spin in 2D cosmological simulations; extruding them to 3D suggests that filaments spin substantially (19). But a convincing picture of whether or not realistic 3D filaments spin is still missing.

We investigate this question using the Millennium 3D dark matter cosmological simulation (20). Although there are other, more dynamical filament definitions (21), we use a simple empirical definition: the matter connecting pairs of dark-matter haloes with mass above $10^{13} h^{-1} M_{\odot}$ (6). A halo of this mass typically hosts a Luminous Red Galaxy (LRG) (22), and we will simply refer to these halo centers as galaxies. We stack the dark-matter velocity fields around filaments, orienting each filament axis with its average spin direction. That is, making $J_{\text{avg}} > 0$; this is the angular momentum projected along the axis, averaged over radial bins, with inverse-variance weighting; see Eq. (S1). Fig. 1 shows the projected matter and angular momentum density $\mathbf{J} = (1 + \delta)\mathbf{r} \times \mathbf{v}$, averaged over 33,951 filaments 6–10 Mpc/ h long. ($1 + \delta = \rho/\bar{\rho}$ is the matter density ρ relative to the mean matter density $\bar{\rho}$, and \mathbf{v} is the velocity.) In addition to the radial infall due to gravity, there is a clear rotational component around the filament axis. These two sum up to the spiral pattern shown in Panel A. The lengthwise view (B) shows that, on average, the pattern is coherent across the filament. The rotational velocities close to the two galaxies are small (C); it seems that for this sample of rather large galaxies, rotations of their host dark matter haloes are not particularly aligned on average with that of the filaments. In the filament region (between the galaxies, but with distance along the filament > 1 Mpc/ h from both – see Fig. S1), the average rotational velocity peaks at around 80 km/s near the filament axis, but in the galaxy region (outside the filament region), it is much smaller (D). Beyond 3 Mpc/ h from the filament axis, the rotational velocity becomes similar in the two cases, indicating that the galaxies and their filament live in a common large-scale environment, with some rotation. We find that for the innermost bin, the period of rotation is of order the age of the Universe, befitting the Universe’s longest spinning objects. The period may be shorter for a filament definition more closely tracking the density ridge between galaxies. In summary, we have found that these intergalactic filaments rotate.

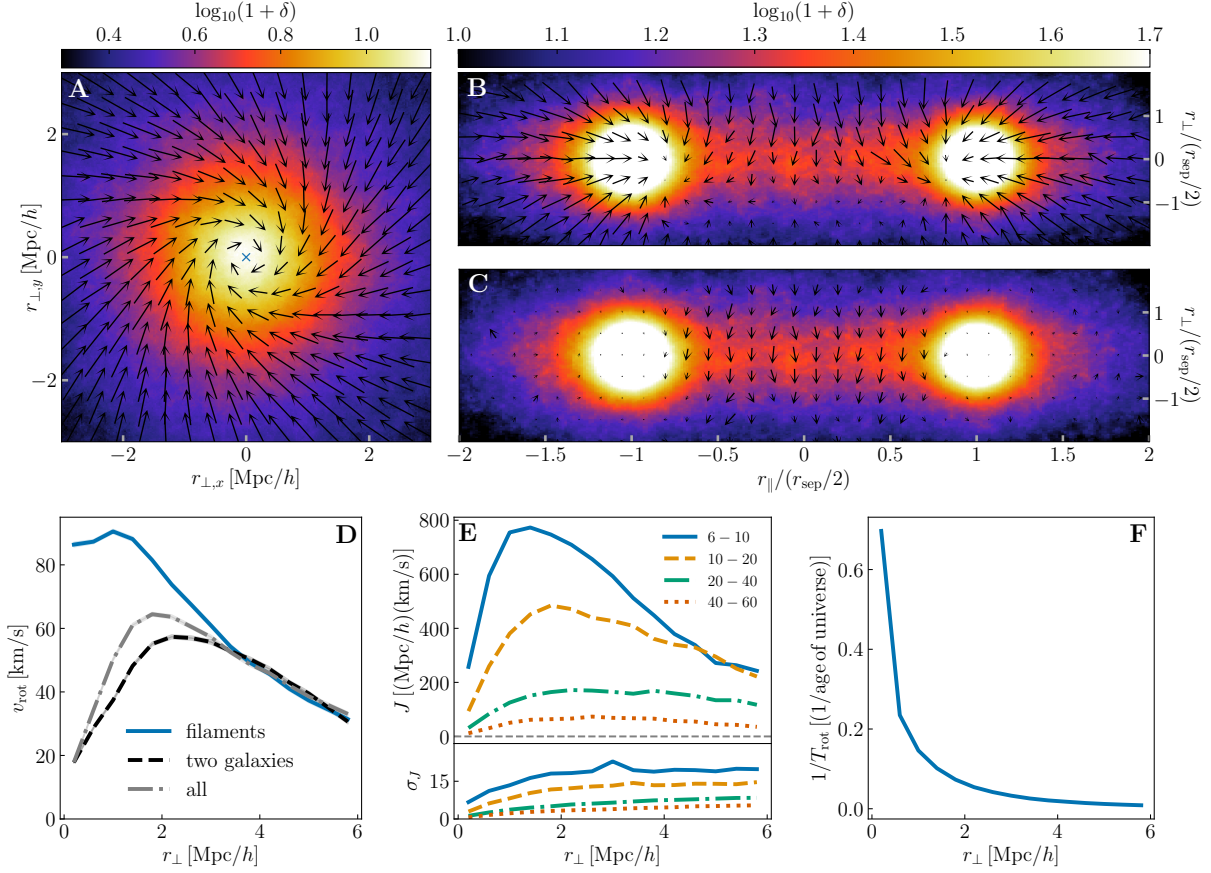


Figure 1: *Top panels: Average density and angular-momentum density fields around filaments.* Colors show the average density around filaments connecting pairs of galaxies separated by 6-10 Mpc/h found in the Millennium simulation. See Fig. S1 for a diagram. (A) Arrows show the angular momentum density \mathbf{J} in the filament region, projected along the filament axis, excluding the galaxy regions. The longest vector corresponds to 1380 (Mpc/h)(km/s). (B) Lengthwise view of \mathbf{J} on one side of the filament axis, stacked over filaments (rescaling coordinates so each galaxy lies at ± 1), and projected. Here, arrows show \mathbf{v} instead of \mathbf{J} , for clarity at large $1 + \delta$. The longest vector corresponds to 264 km/s. (C) Same as (B), but with radial infall velocities around two haloes nulled (See §S1.3). *Bottom panels: (D) Rotational velocity profile.* Average azimuthal velocity v_{rot} as a function of distance to the filament axis r_{\perp} , in the filament region and the galaxy regions as shown in panel B. Matter in the filament region (blue) exhibits stronger rotation around the filament axis than in galaxy regions (black). (E): **Filament angular momentum density profile, $J(r_{\perp})$.** The upper panel compares $J(r_{\perp})$ for different filament lengths in units of Mpc/h. Signals from random patches of the same length in the simulation have been subtracted for each case. The lower panel shows their corresponding errorbars. Details for the error estimation can be found in Eq. (S4). (F): **Period of rotation.** At $z = 0$, a full rotation near the center would need of order the age of the Universe. In the innermost bin, 34% have period less than the age of the Universe.

To test if the filament-rotation signal might arise from random velocity flows, we repeated the measurement around pairs of random positions with the same separations as the galaxies. The average angular momentum density profile $J(r_{\perp})$ in the random filaments is positive, to be expected since it is on average aligned with J_{avg} in the same way as in the real sample, but in the randoms it is much smaller. Panel E of Fig. 1 shows that $J(r_{\perp})$ from filaments is significantly higher than zero, after subtracting the signal from random filaments. For a plot showing both reals and randoms without the subtraction, see Fig. S4, using a warm dark matter simulation, with similar results as in the Millennium. In summary, angular momenta of real filaments are much larger than those of randoms.

To investigate how the signal varies with the filament length, we repeated the measurement for several length ranges. We find that the rotation decreases for longer filaments, becoming very small at 40-60 Mpc/ h (Panel E). This is expected, since pairs of galaxies at this large separation rarely have nearly straight-line physical density ridges connecting them (6).

This coherent filament rotation has not before been measured, to our knowledge. However, an important, relevant aspect of the velocity field around a filament that has been previously studied is an alternating-sign quadrupolar spin field pattern (13), also related to a quadrupolar vorticity field around filaments at the current epoch (17, 23). This arises, e.g., from the curl-free, gravitationally-sourced velocities of an elliptical density peak (§S1.8); also see Fig. 3. The orientation of each filament cross-section is random in Fig. 1, averaging out any such pattern, so we also try orienting the stack along the major axis (the largest eigenvector) of the projected matter distribution around each filament. The density concentration along the x -axis indicates a wall on average, within which the filament is embedded (left panel in Fig. 2). In Fig. 2 (middle), it is clear that the monopole (isotropic) part of the angular momentum density dominates over the anisotropic part. Subtracting the isotropic signal (measured from the left panel of Fig 1) reveals a quadrupole pattern (right panel in Fig 2). The white zero contours grow vertical and horizontal at large radius, as expected (13). But closer to the filament, the quadrupole is $\sim 45^\circ$ rotated, perhaps from the matter flow overshooting the filament with some impact parameter.

The monopole we find is not present in the primordial, irrotational velocity field of the simulation. Integrating a zero-curl field around a circle, the angular momentum vanishes. Where, then, does the rotation at a later time come from? This is well-understood (24); to illustrate it, we use a 2D cosmological simulation to track the evolution of angular momentum around 2D haloes, which correspond to ideal filaments in 3D (see §S1.2) for more details, and movie (25) for illustration.). The reason for using a 2D instead of 3D simulation is that the center of a

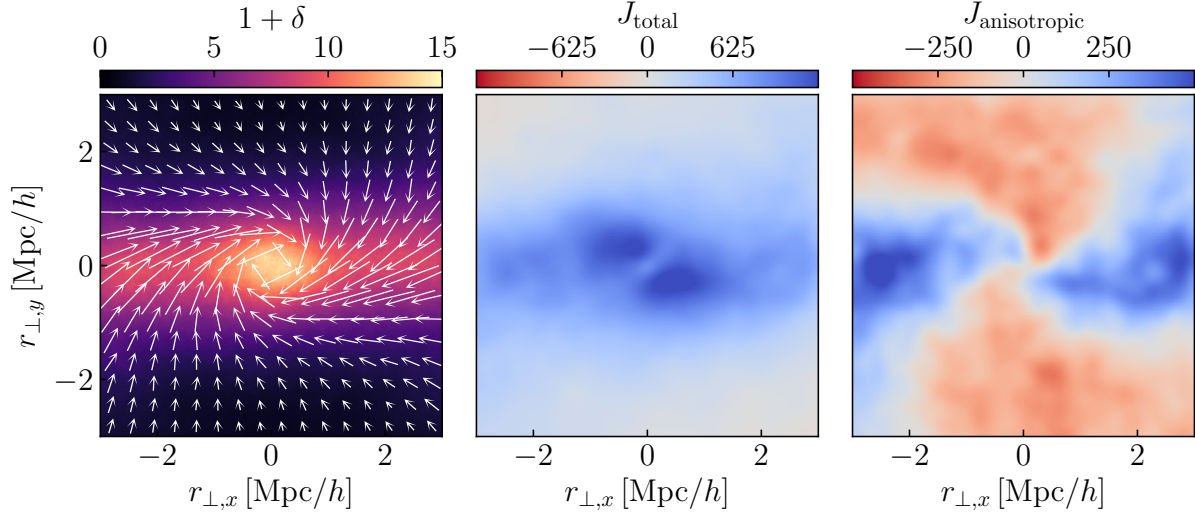


Figure 2: *Left panel:* Average density (colors) and angular-momentum density fields (vectors) as in Fig. 1A, but stacked so that walls in which each filament is embedded will appear horizontally. The maximum length of vectors corresponds to $1760 \text{ (Mpc/h)(km/s)}$. *Middle panel:* Magnitude of angular-momentum density with the positive direction defined as into the paper. *Right panel:* Angular-momentum density with the isotropic component subtracted.

2D halo, which corresponds to a point along the axis of a 3D filament, can be easily tracked throughout its evolution history. In 3D, such a point is difficult to track in time, especially with merging and mixing along the filament. Initially, the angular momentum has a clear quadrupolar pattern in the center (Panel A of Fig. 3), summing to zero around circles. At the outskirts, though, the boundary of the protofilament is not circular, giving a net angular momentum (Panel B) (24). As this matter falls onto the filament, pulled by gravity, it carries this angular momentum to the filament axis. Collapsed particles, identified by (26), appear randomly arranged, losing their initially obvious quadrupole (Panel C). In Panel D, we quantify the evolution of the monopole for a stacked sample of 183 such haloes in the simulation. As time passes, the averaged angular momentum is transported from the outskirts towards the center. It is also clear that collapsed particles contribute most to the angular momentum near the center of the filament, whereas non-collapsed particles dominate the angular momentum at the outskirts. Near the filament center, the ratio between the monopole and quadrupole is zero initially, but then increases with time as the monopole increases and the quadrupole diminishes. In summary, angular momentum around filaments originates in analogy to the tidal-torque theory (27, 28) for galaxies: an asymmetric matter distribution is torqued up and is later transported gravitationally

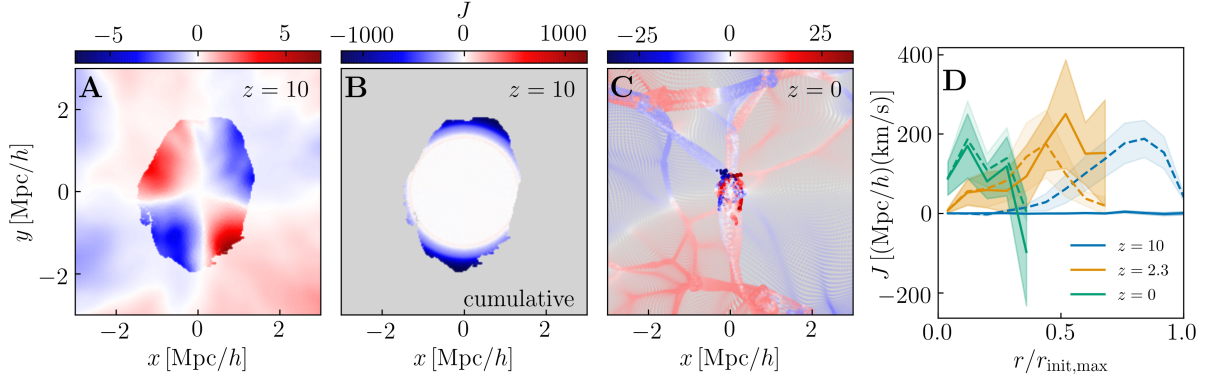


Figure 3: Evolution of angular momentum J . The evolution of angular momentum around a 2D halo (roughly, a cross-section of a 3D filament) from a 2D simulation. Colorbars in Panels A-C apply to the angular momentum J . In Panels A & C, particles in the simulation that collapse to a halo are shown with bright, and non-collapsed particles are shown with muted colors. (A) At $z = 10$, the quadrupole pattern is clear both for the protohalo region and the surroundings. (B) The cumulative net angular momentum of particles, summed from the center, shows that J originates at the outskirts of the region that later collapses. (C) The quadrupole randomizes during evolution from $z = 10$ to the current epoch (for clarity, J for the outer particles has been transformed to $\sinh^{-1}(J/10)/2$.) (D) The average angular momentum in radial bins from 183 such 2D haloes at three different epochs shown in the legend. We see the angular momentum being transported to the center. Here $r_{\text{init,max}}$ is the largest comoving distance from the area centroid to a particle in the initial conditions, and r is in comoving coordinates. Solid curves include all particles, while dashed curves include only particles that are collapsed at $z = 0$. The shaded regions represent the error on the mean.

to the center. As with galaxies and their dark-matter haloes (28, 29), the angular momentum of a filament cross-section seems to grow as the scale factor $a^{3/2}$ until collapse, after which angular momentum is conserved in physical coordinates, generally retaining its direction (19).

The above results demonstrate that on average, filaments rotate, but what fraction of individual filaments can be said to rotate? We use the average spin J_{avg} to quantify this. $J_{\text{avg}} > 0$ by definition, so at some level, all filaments rotate, just as all galaxies spin (have nonzero spin). But the physically relevant question is, what fraction substantially rotate? To answer this, we compare distributions of J_{avg} in filaments, and in random line segments of the same length, shown in Fig. S2. We fiducially define a filament as ‘substantially rotating’ if its J_{avg} exceeds 95.5% (a $2\text{-}\sigma$ level) of the randoms. According to Fig. S2, 26% of real filaments exceed this level, and therefore substantially rotate. This depends on the threshold, though; see §S1.5 for more details. Another question is to what degree do the filaments that we investigate corre-

spond to collapsed objects? Using a warm-dark matter simulation, we find that the contribution of collapsed particles to filaments defined in our empirical way is much higher than in random line segments (§S1.7). This suggests that our results would hold if we used a filament definition requiring coherent, collapsed structures, as well.

Detecting filament rotation in the observed Universe will be challenging, but possible. The most straightforward way may be to identify thick filaments of galaxies between clusters; one could look for rotation in the galaxies and gas between them (30). For a rotating filament nearly in the plane of the sky, on average, one side will move away, and the other toward, the observer (Fig. 1B). Suppose observed galaxies in such a filament are stacked as in Fig. 1A. Redshift-space distortions would cause anisotropy in this galaxy-density profile, whether from random motions as in cluster fingers of god, or from infall (31). Rotation on top of this would shear this profile, somewhat tilting the major axis of an elliptical fit to it away from the line of sight or the plane of the sky. In analogy to viewing a rotating galaxy edge-on, this stacked distribution would have a redshift dipole.

Also, the ionized gas around the filament, likely co-rotating with the dark matter and galaxies, should scatter photons from the cosmic microwave background (CMB) in opposite directions in the two sides, by the kinematic SunyaevZeldovich (kSZ) effect. This would cause a dipole extending along the filament axes, imprinted on the CMB temperature map. It might be measured in a manner similar to how the kSZ effect has been detected around galaxies and galaxy clusters (32, 33).

Also, spin correlations between nearby galaxies (34) could be interpreted as a suggestion of filament spins. We find that galaxies on the ends of filaments tend not to co-rotate particularly with them in Fig. 1, but the haloes hosting these galaxies are rather large-mass; possibly, smaller galaxies within larger-scale filaments would tend to co-rotate more.

It remains to study how baryonic gas rotates within filaments. Gas is subject to shocks and galactic feedback, adding stochasticity. On the other hand, gas tends to be smoother than the dark matter (35), so many gas filaments might rotate quite coherently. Filamentary gas since reionization is typically ionized, so if any processes might act differently on electrons and protons in filaments, e.g. in a Biermann battery mechanism (36–38), rotation would generate a coherent magnetic field along the filament axis. A model with rotation in addition to shocks could help to understand the origin of cosmological seed magnetic fields. Also, an observational indication of a rotating filament could be a coherent magnetic field aligned with it, probed through e.g. synchrotron emission or Faraday rotation of a background polarized source (30).

Our finding is consistent with the standard tidal-torque understanding of the origin and evolution of angular momentum in large-scale structure. Net angular momentum arises from velocities on the outskirts of collapsing structures, and gets transported to the center by gravity. The net rotational velocity around a filament, an addition to the known quadrupolar pattern, is likely to influence the spin of galaxies in the vicinity of filaments. In particular, the picture of rotating filaments helps to explain why small haloes embedded in filaments tend to align their spins with their filament directions (11).

Our results indicate that the longest coherently rotating objects in the Universe are likely filaments. Candidates for this title include cosmic-web components: dynamically-defined haloes, filaments, walls, and voids. Haloes, including the largest galaxy clusters, rotate, but filaments can be much longer. Walls and voids have similar lengths as filaments, and even substantial widths or depths. However, walls, and especially voids, are unlikely to rotate as substantially and coherently as the rotating filaments (see §S1.9). It remains to find them.

Acknowledgments

We acknowledge stimulating discussions with John Peacock, Catherine Heymans, Andy Taylor, Cheng Si, David Essex, and Beth Biller. Part of this work used the DiRAC@Durham facility managed by the Institute for Computational Cosmology on behalf of the STFC DiRAC HPC Facility (www.dirac.ac.uk). The equipment was funded by BEIS capital funding via STFC capital grants ST/K00042X/1, ST/P002293/1 and ST/R002371/1, Durham University and STFC operations grant ST/R000832/1. DiRAC is part of the UK National e-Infrastructure. **Funding:** QX acknowledges support from the European Research Council under grant number 647112. MCN is grateful for funding from Basque Government grant IT956-16. YC acknowledges the support of the Royal Society through the award of a University Research Fellowship and an Enhancement Award. MAAC acknowledges support from Mexican grant DGAPA-PAPIIT IA104818. **Competing Interests:** The authors have no competing interests. **Author Contributions:** QX performed all measurements and quantitative analysis, contributing to writing and ideas for methodology. MCN and YC conceived of the project, and led the analysis and writing. MAAC contributed simulation data and essential discussions.

S1 Materials and Methods

S1.1 The Millennium simulation

Our main results are based on analysis using the Millennium simulation (20). It is a dark-matter-only cosmological N-body simulation, using 2160^3 dark matter particles to represent the matter distribution of a model universe in a cube of $500 \text{ Mpc}/h$ on a side. Each dark-matter particle has mass $8.6 \times 10^8 h^{-1} M_\odot$. The simulation was run in a standard Λ CDM model with the following cosmological parameters: $\Omega_m = 0.25$, $\Omega_b = 0.045$, $h = 0.73$, $\Omega_\Lambda = 0.75$, $n_s = 1$ and $\sigma_8 = 0.9$. For the purpose of fast computation, we randomly downsampled to one-tenth the original particle density.

Dark matter haloes are first detected in the simulation with a Friends-of-Friends (39) method, at the first step resulting in the same halo sample as Millennium halo catalogs in its database (40). We define galaxy position within a halo with the location of its most-bound particle, involving a Spherical Overdensity approach. See (41) for further details. We use haloes with mass greater than $10^{13} h^{-1} M_\odot$ to represent Luminous Red Galaxies (LRGs) (22, 42), assuming that each halo hosts one galaxy. We choose this galaxy type because it is well-characterized observationally, the target of many large-scale-structure surveys, e.g. (43). We end up with 35,300 simulated galaxies in the simulation box. We then identify in total 33,951 pairs of galaxies separated by 6-10 Mpc/h to be our fiducial sample. This distance range is chosen so that the galaxies are substantially farther apart than their own haloes, of size $\sim 1 \text{ Mpc}/h$, but are near enough to typically be connected by a coherent dark-matter filament (6). What does a ‘coherent dark-matter filament’ mean? There is not a universally agreed-upon, strict definition of this (21), but our conception, shared by many, is a nearly straight density ridge (44) between the two galaxies. We expect that within such a density ridge, dark-matter streams have crossed, i.e. initially distant dark matter particles have come together in the same place, moving at different velocities, possible for such a collisionless fluid (26). Also, that gas has shocked (the baryonic version of stream crossing). We expect that most of our filaments, defined simply as straight line segments between LRGs in this length range, conform to this definition; some observational evidence supports this (7, 45–48). For comparison, we also select longer filaments as follows: 10-20, 20-40, and 40-60 Mpc/h . Measurements for the angular momentum around these filaments are presented in Fig. 1.

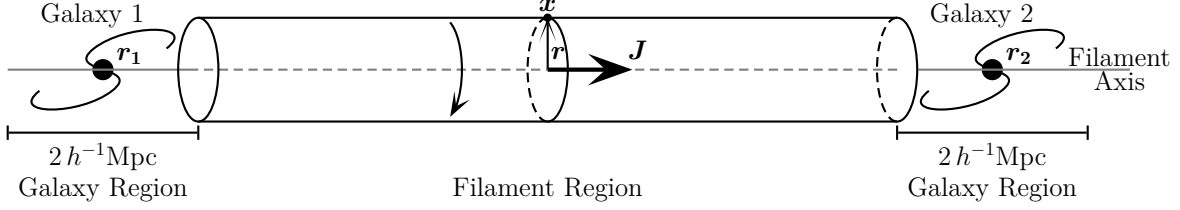


Figure S1: Illustration of coordinates for the galaxy-filament system. The line connecting the two galaxies at \mathbf{r}_1 and \mathbf{r}_2 is defined as the filament axis. The filament region is defined to be $1 \text{ Mpc}/h$ away from each galaxy, to isolate the filament signal from possible contamination from the galaxies' dark matter haloes. The average angular momentum \mathbf{J}_{avg} (see Eq. S1) for an individual filament defines the direction of the spin.

S1.2 2D Simulation

To understand the collapse of matter onto a cross-section of a filament, we use a two-dimensional N -body simulation. It was previously used in Ref. (19), with some analysis and animations (see https://youtu.be/7KjesL_hP7c) relevant to the present work. We detect haloes in the 2D simulation using the ORIGAMI algorithm (26). A particle is classified as a halo particle if, going from the initial to final conditions, it has ‘folded’ (crossed some other particle) along two (in 2D) initial orthogonal axes. We then join together groups of particles adjacent on the initial Lagrangian square grid to form haloes.¹

S1.3 Definitions of filament & stacking

As shown in Figure S1, for each pair of galaxies at positions \mathbf{r}_1 and \mathbf{r}_2 , we define the filament axis as the line connecting them, with the direction $\hat{\mathbf{n}} = \frac{\mathbf{r}_2 - \mathbf{r}_1}{|\mathbf{r}_2 - \mathbf{r}_1|}$. For every particle with position vector \mathbf{x} , $L = (\mathbf{x} - \mathbf{r}_1) \cdot \hat{\mathbf{n}}$ is then the projected distance from \mathbf{r}_1 .

We define the filament region to be the dark matter between the two galaxies, and at least $1 \text{ Mpc}/h$ away from each galaxy along the filament axis to avoid contamination from the dark

¹Several haloes returned in this process were actually groups of haloes apparently distinct by eye, joined by small bridges of halo particles. The spurious fragmentation of filaments into tiny haloes in simulations with truncated initial power (49) likely contributed to this. Applying a mathematical morphology erosion operator cut many of these bridges, returning haloes that generally corresponded to visual expectation. Erosion, used e.g. by Ref. (50), shaves off cells within a specified distance (here, one pixel) of a boundary from all contiguous blobs. We computed the erosion by smoothing the Lagrangian ‘halo’ (1) and ‘not-halo’ (0) field with a circular top-hat filter of radius one pixel; after smoothing, we classified as ‘halo’ particles all corresponding pixels with a value > 0.99 .

matter haloes of the galaxies. The averaged virial radius r_{200} of our halo sample is $0.5 \text{ Mpc}/h$, with its 99 percentile being $\sim 1 \text{ Mpc}/h$. Galaxy regions are the matter within $1 \text{ Mpc}/h$ from their centers along the filament axis. $J = (\mathbf{r} \times \mathbf{v}) \cdot \hat{\mathbf{n}}$. We divide particles into 31 equally spaced cylindrical shells around the filament axis. Here, we choose the spin direction $\lambda = \pm 1$ for a filament so that the (inverse-variance-weighted) average angular momentum over the cylindrical bins is positive. That is, that

$$J_{\text{avg}} = \lambda \sum_{\text{shells } i} \frac{\sum_{\text{particles } k} J_{\text{proj},k;i}}{N_i \sigma_i^2} > 0, \quad (\text{S1})$$

where N_i is the number of particles in the i th cylindrical shell, σ_i^2 is the variance of J over particles in the shell, and the subscript k labels each particle within the shell. Inverse-variance weighting ensures that J_{avg} is a relatively robust quantity to use in determining each filament's orientation.

Having defined coordinates, we measure its density and angular-momentum density fields in rectangular boxes along the axis, and then project these boxes either along or perpendicular to the axis. We rescaled each axis so that the two galaxies are centered at -1 and 1 .

Along the filament axis, we only project particles that are in the filament region, i.e. excluding $1 \text{ Mpc}/h$ along the axis from the center of each galaxy. The result is shown in Panel A of Fig. 1. We can see a clear overall rotation in the projected filament, in addition to an infalling velocity field.

Perpendicular to the filament axis, projecting the whole box width will cancel the coherent rotational velocities. We therefore split each filament along its axis into two halves, and flip the sign of the position coordinates and velocities to make them aligned with the other half. The resulting stacked density and velocity fields are shown in Panel B of Fig. 1. Rotational velocities in the filament regions between the two galaxies are clearly visible. There are also strong infall velocities towards the two galaxies, driven by the gravitational potentials of the two galaxies. Also, note that near galaxies, the places where velocities are zero are off-center from the density peaks. Apparently, the entire system is gravitationally attractive, constituting an overdensity.

In Panel C of Fig. 1, for each galaxy pair with $\lambda = -1$, we flipped the sign of velocities instead of interchanging positions of the pair, before stacking them. This procedure aligns the sense of rotation but flips any infall velocity near the two galaxies. Therefore, when averaged over a large sample, this has effect of almost entirely nulling the radial component of velocities towards the two galaxies.

S1.4 Measuring rotational velocity and angular momentum density

We measure the rotational velocity of dark matter in cylindrical shells for the filament and galaxy regions. For each filament, the rotational velocity in the i th shell is defined as

$$\langle v_{\text{rot}} \rangle_{\text{shell } i;f} = \frac{\sum_{\text{filaments } f} \sum_{\text{particles } k} J_{\text{proj},k;i;f} \cdot \lambda}{\sum_{\text{filaments } f} N_{i;f} r_{\perp,i}}, \quad (\text{S2})$$

where $N_{i,f}$ is the number of particles within the i th shell in the f th filament, and $r_{\perp,i}$ is the perpendicular distance to the i th shell. For the average angular velocity in haloes, we repeat above calculation but for particles that are within $1 \text{ Mpc}/h$ to the haloes.

The angular momentum density in the i th shell is defined as

$$\langle J \rangle_{\text{shell } i} = \frac{\sum_{\text{filaments } f} \sum_{\text{particles } k} J_{\text{proj},k;i;f} \cdot \lambda}{\sum_{\text{filaments } f} R_{\text{sep},i;f} A_i \bar{\rho}}, \quad (\text{S3})$$

where $R_{\text{sep},i;f}$ is the length of filament region, A_i is the area of i th annulus, and $\bar{\rho}$ is the mean density in the simulation.

Results showing measurements as a function of r_{\perp} are shown in Panel D & E of Fig. 1. Errorbars are calculated from the error on the mean of these two quantities among the full filament samples, following

$$\text{Var}(\bar{X}) = \text{Var}\left(\frac{X_1 + X_2 + \dots + X_n}{n}\right) = \frac{\text{Var}(X)}{n}. \quad (\text{S4})$$

S1.5 Rotation signal from random samples

The angular momentum is defined as a positive quantity, as described in the previous two sections. To investigate the significance of the rotational signal, it is essential to know the amplitudes of the signal arising from a random scenario. For this, we define pairs of random points chosen to have the same lengths as the real filament samples. We repeat measurements as shown in the previous sub-section for the angular momentum density profiles for these random samples. For most of the cases we have investigated, the random signal is found to be sub-dominant over the signal from real filaments. The profiles shown in Fig. 1F have had the random signal subtracted off. For the longest filaments ($40\text{--}60 \text{ Mpc}/h$), the residual $J(r_{\perp})$ is very small, indicating that the signal is very close to the random case. See Fig. S4 for a comparison of typical real and random signals, without subtracting off. In estimating the error bars shown, we neglected the small error on $J(r_{\perp})$ measured from the randoms.

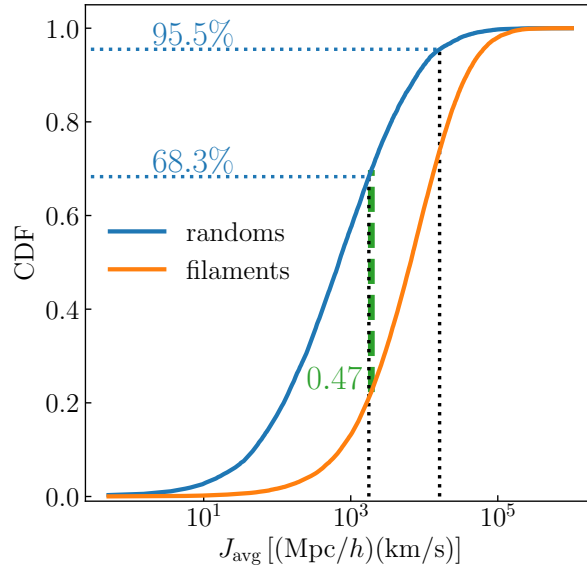


Figure S2: The cumulative distribution functions (CDF's) of the averaged angular momentum J_{avg} for random line segments and filaments. The green dashed line indicates the maximum difference between the CDF's, the D statistic used in a two-sample Kolmogorov-Smirnoff test. The black dotted lines indicate the thresholds corresponding to 68.3% ($1-\sigma$) and 95.5% ($2-\sigma$) probabilities that J_{avg} is not drawn from the J_{avg} distribution of random line segments. In the random sample, the fractions exceeding these thresholds are $1 - 0.683 = 31.7\%$ and $1 - 0.955 = 4.5\%$, to be compared respectively with 79% and 29% of real filaments.

A standard, single summary statistic of the difference between such distributions uses the two-sample Kolmogorov-Smirnov test. We find a maximum vertical separation between the CDFs of $D = 0.47$. For this sample of tens of thousands, the null hypothesis that the two samples are drawn from the same distribution is rejected with essentially certain confidence; the p -value characterizing the probability that the two distributions are the same is $\sim 10^{-120}$.

More tangibly, how might we answer the question of whether an individual filament is substantially rotating or not? We can decide by reference to the distribution of J_{avg} for the random sample. If we define a filament to be ‘rotating’ if its J_{avg} is over a $1\text{-}\sigma$ cut (where 31.7% of the randoms have higher J_{avg}), 79% of the real filaments are rotating. If we are more strict, and define ‘rotating’ with a $2\text{-}\sigma$ cut (where 4.55% of the randoms have higher J_{avg}), 26% of the real filaments are rotating. This $2\text{-}\sigma$, 26% fraction is our fiducial, simple response to the question ‘how often do filaments substantially rotate?’ but it uses an admittedly arbitrary threshold.

S1.6 Co-rotations at different radii

The direction of angular momentum for each filament is defined with an inverse-variance-weighting scheme as described above. There is no guarantee, in principle, that the rotations are perfectly coherent throughout different radii. To check this, we compute the correlation matrix for the rotational velocities $\mathbf{r} \times \mathbf{v}$ at different radii. An example for the 33,951 filaments with 6-10 Mpc/ h separation is shown in Fig. S3. We find that the correlation coefficients between adjacent radial bins are close to unity, indicating that for most filaments, the matter in adjacent cylindrical shells is co-rotating. The coefficient decays with bin separation, as expected.

S1.7 Are the rotating filaments collapsed?

We wish to investigate whether the rotation signal is primarily from particles that have collapsed into a filament. The ORIGAMI (26) algorithm is ideal to identify collapsed filament particles. In a 3D simulation, a particle is tagged as a void, wall, filament, or halo particle if it has crossed 0, 1, 2, or 3 other particles along initial orthogonal axes. Our main results are based on the well-known Millennium simulation, but unfortunately it has glass initial conditions, to which the ORIGAMI algorithm cannot be applied. For this test of how coherently collapsed the rotating filaments we find might be, we use a warm-dark-matter (WDM) dark-matter simulation, presented in Ref. (51). Smoothing the initial conditions produces a more visually prominent

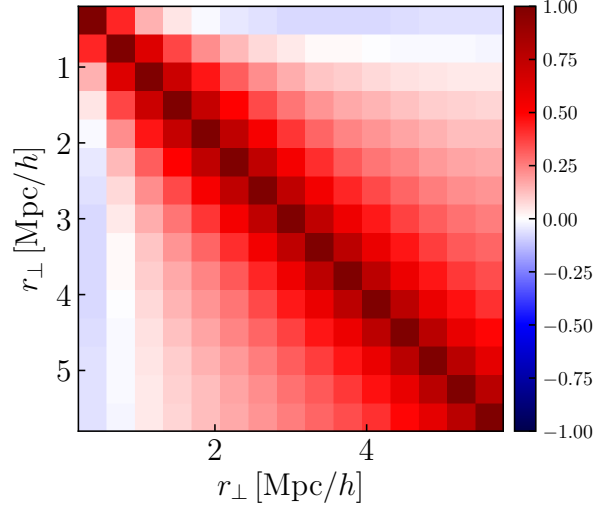


Figure S3: Filament-to-filament correlation matrix of the angular momentum density $J(r_{\perp})$ in different radial bins. Each sample is a single filament with length 6-10 Mpc/h. The positive off-diagonal elements indicate that matter in different radial bins indeed generally co-rotate. This correlation decreases with increasing bin-separation, as expected.

cosmic web. Quantitatively, this cosmic web prominence is evident as a substantial mid-range peak corresponding to walls and filaments in the particle-by-particle density PDF. The ORIGAMI method also particularly shines with smoothed initial conditions (see Fig. 3 of Ref. (52)). The 100 Mpc/h, 512^3 -particle simulation we use had initial conditions smoothed at $\alpha = 0.1$ Mpc/h (but with a gradual kernel, extending a factor of ~ 6 larger in scale).

We identified the haloes used to define filaments in the 3D WDM simulation in a new way, similar to that used for the 2D simulation: we first tagged particles with ORIGAMI (26). We joined together ‘halo’ particles that were adjacent on the Lagrangian grid. We first applied an erosion operator with a radius of one grid spacing, to cut some visually spurious links, and to remove tiny spurious haloes within filaments (49). We used this method because the outer (‘splashback’) caustics of haloes in WDM are more visually evident than in CDM, and the ORIGAMI method worked well to identify these halo boundaries (52). The haloes we used had at least 1000 particles, resulting in a sample of 1825 haloes. Because of the substantial differences in the halo finder, mass estimate, and WDM cosmology, we do not treat this halo sample as equivalent to our Millennium sample, but these results are still relevant.

In Fig. S4, we see that for real filaments in the WDM simulation (left), the signal is dominated by halo particles, with decreasing contributions from filament and wall, and totally un-

collapsed void particles. Note that the ‘halo’ particles are not in the galaxies at the end of the filament, but are in (likely smaller) haloes between them. Also, spurious fragmentation in WDM filaments (49), meant that some filament particles may have been misclassified as halo particles. So, both ‘halo’ and ‘filament’ particles should arguably be classified together, as filament matter that has collapsed. At right, we do the same measurement, except using random filament endpoints instead of haloes. In that case, the contribution from each type is much smaller.

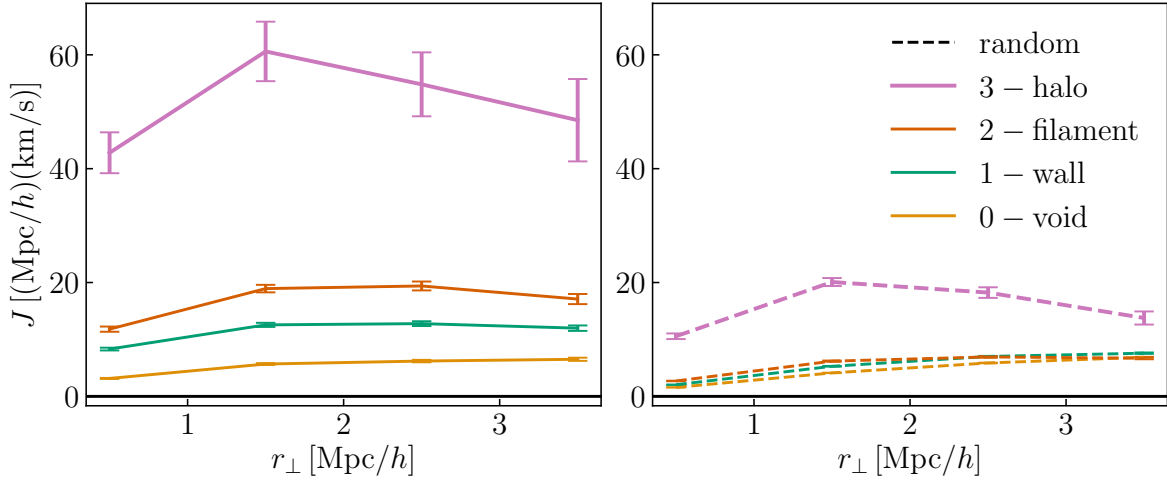


Figure S4: Angular momentum density profile $J(r_\perp)$ contributed from particles with different origami tags (0, 1, 2, 3) in the WDM simulation, for filaments 6-10 Mpc/h long (Left) and for a random sample with the same length (Right). The tags, in increasing order, indicate the degree of collapse, i.e. 0 (voids) – uncollapsed, 1 (wall) – collapsed along one axis, 2 (filament) – collapsed along two axes, 3 (halo) – collapsed along three axes. $J(r_\perp)$ increases as the degree of collapse increases. Error bars indicate the error on the mean in all cases.

S1.8 Quadrupole from elliptical density peak

To illustrate a simple situation in which a quadrupolar pattern of angular momentum arises, we set up a 2D elliptical density peak as shown in the left-hand panel of Fig. S5. We use the Zel’dovich approximation (53) to estimate the gravitationally sourced velocity from this, taking the gradient of the inverse Laplacian of the 2D density field. Note that these velocities are exact in the initial conditions, and should be good approximations on large scales at the late-time Universe. Finally, we compute the angular momentum density using the modeled density and velocities. The result is shown in the right-hand panel of Fig. S5. We recover a quadrupole,

with no sign of a monopole, as reported in (13). According to this model, a monopole cannot

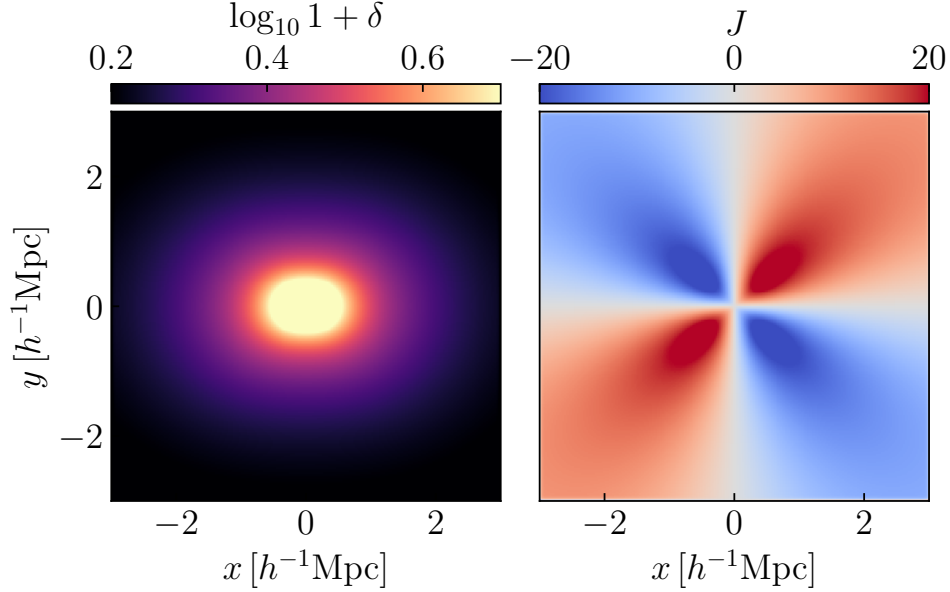


Figure S5: An idealized elliptical density peak (Left). The gradients of its gravitational potential give rise to a quadrupolar pattern of angular momentum density (Right).

arise from the gravity sourced by a perfectly elliptical density peak; indeed, it cannot from any irrotational flow (from a gravitational potential).

S1.9 Candidates for the longest rotating objects in the Universe

It is helpful to define ‘object’ in our statement that the longest coherently, substantially rotating objects in the Universe are likely filaments. An ‘object’ is a cosmic-web component; a coherent virialized or collapsed object (halo, filament, or wall), or a region without collapse (void). For definiteness, we assume a dynamical dark-matter-sheet folding definition of these objects (26), but some other definitions broadly agree, e.g. (54); see (21). The point is that this definition does not encompass a supercluster, which would contain many virialized haloes, without being virialized itself.

The largest of these objects, with three large dimensions, are the roughly polyhedral voids. Voids are ‘cosmic magnifiers,’ their interiors expanding faster than the cosmic mean (55), resulting in zero vorticity (56), and with no coherent rotation expected. Moving to lower volume, walls have two large dimensions. They may contain rotating patches (haloes and filaments

within them). However, they are unlikely to rotate coherently as a disk, since they evolve similarly to voids in a 2D universe, being less dense than their surrounding filaments. They, too, often expand faster than the cosmic mean (57), thus dampening vorticity normal to their surface. Still, it remains to study coherent rotation in walls. As for haloes, they are well-known to spin, but are of maximum radius (as measured from the Millennium haloes) $\sim 2 \text{ Mpc}/h$.

Another, merely suggestive argument for filaments as the longest objects is that in the toy, origami approximation (58) (18), filaments, extrusions of 2D origami twist folds, are the largest rotating components; walls and voids do not rotate. In the real Universe, ambiguity exists; patches likely exist that straddle the clear categories of wall, filament, and halo. Another caveat is that our measurement is based on a simple empirical, not dynamical definition of a filament. However, §S1.7 supports the idea that these definitions are often equivalent from the point of view of rotation, at least for $6\text{--}10 \text{ Mpc}/h$ filaments. In conclusion, the longest rotating objects in the universe are likely filaments.

References

1. A. A. Klypin, S. F. Shandarin, *MNRAS* **204**, 891 (1983).
2. J. R. Bond, L. Kofman, D. Pogosyan, *Nat* **380**, 603 (1996).
3. V. de Lapparent, M. J. Geller, J. P. Huchra, *ApJ* **302**, L1 (1986).
4. M. Colless, *et al.*, *MNRAS* **328**, 1039 (2001).
5. I. Zehavi, *et al.*, *ApJ* **736**, 59 (2011).
6. J. M. Colberg, K. S. Krughoff, A. J. Connolly, *MNRAS* **359**, 272 (2005).
7. J. Clampitt, H. Miyatake, B. Jain, M. Takada, *MNRAS* **457**, 2391 (2016).
8. M. A. Aragón-Calvo, R. van de Weygaert, B. J. T. Jones, J. M. van der Hulst, *ApJ* **655**, L5 (2007).
9. O. Hahn, C. Porciani, C. M. Carollo, A. Dekel, *MNRAS* **375**, 489 (2007).
10. D. J. Paz, F. Stasyszyn, N. D. Padilla, *MNRAS* **389**, 1127 (2008).
11. E. Tempel, N. I. Libeskind, *ApJ* **775**, L42 (2013).

12. Y. Dubois, *et al.*, *MNRAS* **444**, 1453 (2014).
13. S. Codis, C. Pichon, D. Pogosyan, *MNRAS* **452**, 3369 (2015).
14. P. Ganeshaiah Veena, *et al.*, *MNRAS* **481**, 414 (2018).
15. K. Kraljic, R. Davé, C. Pichon, *MNRAS* p. 237 (2020).
16. S. Codis, *et al.*, *MNRAS* **427**, 3320 (2012).
17. C. Laigle, *et al.*, *MNRAS* **446**, 2744 (2015).
18. M. C. Neyrinck, *MNRAS* **460**, 816 (2016).
19. M. Neyrinck, M. A. Aragon-Calvo, B. Falck, A. S. Szalay, J. Wang, *The Open Journal of Astrophysics* **3**, 3 (2020).
20. V. Springel, *et al.*, *Nat* **435**, 629 (2005).
21. N. I. Libeskind, *et al.*, *MNRAS* **473**, 1195 (2018).
22. G. Zhu, *et al.*, *MNRAS* **439**, 3139 (2014).
23. C. Pichon, F. Bernardeau, *A&A* **343**, 663 (1999).
24. A. G. Doroshkevich, *Astrophysics* **6**, 320 (1970).
25. Movie for illustration https://youtu.be/7KjesL_hP7c.
26. B. L. Falck, M. C. Neyrinck, A. S. Szalay, *ApJ* **754**, 126 (2012).
27. P. J. E. Peebles, *ApJ* **155**, 393 (1969).
28. S. D. M. White, *ApJ* **286**, 38 (1984).
29. P. Motloch, H.-R. Yu, U.-L. Pen, Y. Xie, *arXiv e-prints* p. arXiv:2003.04800 (2020).
30. G. Brunetti, F. Vazza, *Phys. Rev. Lett* **124**, 051101 (2020).
31. N. Kaiser, *MNRAS* **227**, 1 (1987).
32. Planck Collaboration, *et al.*, *A&A* **594**, A27 (2016).

33. S. Bocquet, *et al.*, *ApJ* **878**, 55 (2019).
34. A. Slosar, *et al.*, *MNRAS* **392**, 1225 (2009).
35. A. G. Harford, A. J. S. Hamilton, *MNRAS* **416**, 2678 (2011).
36. R. M. Kulsrud, R. Cen, J. P. Ostriker, D. Ryu, *ApJ* **480**, 481 (1997).
37. N. Y. Gnedin, A. Ferrara, E. G. Zweibel, *ApJ* **539**, 505 (2000).
38. S. Naoz, R. Narayan, *Phys. Rev. Lett* **111**, 051303 (2013).
39. M. Davis, G. Efstathiou, C. S. Frenk, S. D. M. White, *ApJ* **292**, 371 (1985).
40. G. Lemson, t. Virgo Consortium, *arXiv e-prints* pp. astro-ph/0608019 (2006).
41. Y.-C. Cai, N. Kaiser, S. Cole, C. Frenk, *MNRAS* **468**, 1981 (2017).
42. J. K. Parejko, *et al.*, *MNRAS* **429**, 98 (2013).
43. K. S. Dawson, *et al.*, *AJ* **145**, 10 (2013).
44. T. Sousbie, *MNRAS* **414**, 350 (2011).
45. S. D. Epps, M. J. Hudson, *MNRAS* **468**, 2605 (2017).
46. A. de Graaff, Y.-C. Cai, C. Heymans, J. A. Peacock, *Astronomy & Astrophysics* **624**, A48 (2019).
47. Q. Xia, *et al.*, *A&A* **633**, A89 (2020).
48. H. Tanimura, *et al.*, *MNRAS* **483**, 223 (2019).
49. J. Wang, S. D. M. White, *MNRAS* **380**, 93 (2007).
50. E. Platen, R. van de Weygaert, B. J. T. Jones, *MNRAS* **380**, 551 (2007).
51. L. F. Yang, M. C. Neyrinck, M. A. Aragón-Calvo, B. Falck, J. Silk, *MNRAS* **451**, 3606 (2015).
52. M. C. Neyrinck, *MNRAS* **427**, 494 (2012).

- 53. Y. B. Zel'Dovich, *A&A* **500**, 13 (1970).
- 54. M. Cautun, R. van de Weygaert, B. J. T. Jones, *MNRAS* **429**, 1286 (2013).
- 55. M. A. Aragon-Calvo, A. S. Szalay, *MNRAS* **428**, 3409 (2013).
- 56. O. Hahn, R. E. Angulo, T. Abel, *MNRAS* **454**, 3920 (2015).
- 57. M. A. Aragon-Calvo, J. Silk, A. S. Szalay, *MNRAS* **415**, L16 (2011).
- 58. M. C. Neyrinck, *The Zeldovich Universe: Genesis and Growth of the Cosmic Web*, R. van de Weygaert, S. Shandarin, E. Saar, J. Einasto, eds. (2016), vol. 308 of *IAU Symposium*, pp. 97–102.